Design and Simulation of an Optimized Biaxial Cruciform Specimen

Abdul Mateen Mohammed*[1] and Deepak B[2]
[1, 2] Department of Mechanical Engineering, School of Engineering and Technology, CMR University, Bangalore, India
(E-mail: mateen.m@cmr.edu.in, deepak.b@cmr.edu.in)

ABSTRACT

The ability to obtain reliable biaxial test data on composite materials is based on the development of an appropriate cruciform specimen design. The best sample should be able to evenly spread stress and strain throughout the central gauge area and avoid early failure at the arm-gauge junctions. This paper aims at overcoming this difficulty by automating the geometric optimisation task using a finite element analysis alongside the Taguchi design-of-experiments approach. The geometric parameters being studied are (i) fillet radius and (ii) spline-controlled arm-gauge transition dimensions, which are varied in a systematic way to study their effects on uniformity of the stresses under equi-biaxial loading. A quarter-symmetry finite element model was established to evaluate nine distinct geometric configurations using the Taguchi L9 orthogonal array. The configurations have been analysed in the ABAQUS software platform with continuum shell elements and the Hashin damage initiation criteria. The following five measures of suitability were evaluated in the 20 x 20mm gauge area: Coefficients of variation (CV) of in-plane stress S_{11} and S_{22}, coefficient of variation of biaxiality ratio S_{22}/S_{11}, coefficient of variation of surface strains, stress concentration factor at the arm-gauge interface, and location of failure against the gauge boundary. Three set-ups were discarded because of failure initiation that was confirmed to be beyond the gauge boundary. The best geometry attained a stress-uniformity CV of 8.4 percent, a biaxiality-ratio CV of 7.9 percent, and an SCF of 1.50, with all the damage being localized to the gauge region. These findings indicate that the use of spline-controlled transition profiles together with a sufficiently large fillet radius would yield a significantly smoother biaxial stress state compared to a sudden transition or entirely circular transition. The geometry and assessment framework suggested, therefore give a reproducible standard in the design of cruciform specimens in the characterisation of laminated composites.

Keywords: Biaxial testing, cruciform specimen, geometry optimization, finite element analysis, Taguchi method, composite laminates

1. Introduction:

The in-plane stresses frequently do not occur along a single major direction in the structural components and more advanced engineering materials, especially in composite laminates, where loading conditions are often biaxial. Such conditions demand reliable constitutive characterization using experimental methods that are capable of applying controlled and well-defined biaxial stress-strain states. The most common configuration is the cruciform specimens, which are now commonly used in testing biaxial in-plane, since they can be loaded in two orthogonal directions with the material being centralized to facilitate material characterization. One of the essential conditions of the cruciform testing is the attainment of a uniform and stable stress-strain field in the gauge region. It has been clearly stated that the strain distribution of cruciform specimens is extremely sensitive to the geometric discontinuity at the arm-gauge joint, which may result in strain localization, parasitic shear, and early failure out of the desired gauge zone [1]. Initial optimization works focused predominantly on local geometrical considerations

S. Uppapalli and D. Chakraborty (eds.), *Proceedings of the International Conference on Mechanics, Materials and Mechatronics (ICM³ 2026)*, Atlantis Highlights in Engineering 47,
https://doi.org/10.2991/978-94-6239-764-4_12

like fillet radius, gauge thinning, and slit designs in an attempt to minimize stress concentration at the arm gauge intersection and slow down the occurrence of premature failure [1]. Although these methods are useful in resolving local stress concentration, they do not have much control over the global load- transfer direction into the gauge region, which is decisive in controlling spatial strain uniformity during biaxial loading. This sensitivity has been reinvestigated (especially in composite laminates) by recent experimental studies, with biaxial stability and failure behavior being demonstrated to be highly dependent on cruciform geometry and uniformity of strain-fields. These observations reiterate the fact that geometry-based design is critical in supporting dependable biaxial tests.

Recent studies have been undertaken in the field of utilizing shape and topology optimization methods to improve the performance of cruciform specimens by changing their overall geometry. Chen et al. reported that topology-shape optimization proved to be an effective approach in decreasing stress concentration and strain non-uniformity in biaxally loaded biaxial loaded cruciform specimen [2]. Similar growths in gauge-field consistency over the global geometrical modifications were reported by Makris et al. [3], and the quality of biaxial gauge-field quality through optimization-based design studies was found to be sensitive to transition geometry and load-path properties [9]. Kim et al. also demonstrated that strain homogeneity in a multiaxial loading condition can be improved by numerical optimization of the cruciform geometry [4]. Despite these promises, such methods usually operate on complicated optimization models and give geometries that are hard to parameterize, recreate, or make in the treatment of experiment validation.

Simultaneously, design-of-experiments (DOE) techniques such as Taguchi orthogonal arrays have been used to optimize cruciform specimens so that exploration of parameters can be systematically done with fewer computational requirements. Lu et al. have determined the fact that the orthogonal experimental design in combination with finite element analysis is an effective way to determine the biaxial performance, thus explaining the effect of the parameters of cruciform geometry on the performance [5]. However, most studies by DOE focus on single-response targets or multiple responses separately, which can present some vagueness in the choice of the best designs and are not fully statistically validated. In addition to geometrical aspects, recent studies have placed a lot of focus on gauge-field validity and equilibrium consistency in biaxial characterization through the use of the cruciform. Vitucci emphasized that maintenance of good biaxial testing needs field-based design and assessment standards, stress and strain field, which meets equilibrium in the gauge area, a necessary restriction to geometrical smoothing [8]. This view highlights the necessity of optimization programs that consider the performance of the cruciform in terms of gauge-field-based measures instead of the peak values in isolation that are mesh-dependent or otherwise of physical interest.

In this context, the current paper contributes towards the interpretation and reproduction of a physically understandable and reproducible optimisation algorithm to design biaxial cruciform specimens. It uses a spline-parameterised arm-gauge transition that directly separates discretionary control of local curvature, through the use of fillet radius, and global load-path layout, via spline control parameters, and therefore permits the stress-smoothing and load-transfer to the gauge region to be systematically modulated. The optimisation of the cruciform specimen geometry was conducted using a Taguchi L9 orthogonal array, incorporating four design parameters each at three levels. Rather than analysing each performance metric independently, the Grey Relational Analysis (GRA) framework was applied to convert the multi-objective problem into a single, scalar Grey Relational Grade (GRG), which was then used as the unified Taguchi response. This approach enables a single main effects plot to capture the simultaneous influence of each design factor across all four objectives—minimising the Hashin fibre-tensile failure index (FIft), minimising the Hashin matrix-tensile failure index (FImt), maximising the gauge-zone stress uniformity ratio, and minimising the 95th-percentile maximum principal strain—weighted according to their relative failure criticality (w = 0.35, 0.25, 0.25, 0.15, respectively).

2. Materials and Methods

In the present study a cruciform specimen with uniform thickness and uniform overall dimension was subjected to a pure in plane biaxial test. The only variation was by parameterising the inner arms and the central gauge region. This was done by modifying the inner arm–gauge transition profile via a spline-based representation for controlled, smooth curvature variations. Contrary to conventional cruciform specimens that employ straight tapers, simple fillets, or cut-outs, the present study utilized a C^2-continuous spline to define the inner boundary of each arm. The use of a C^2-continuous profile guarantees continuity of both slope and curvature, thereby eliminating abrupt geometric transitions. This spline-based approach provides direct control over the curvature distribution along the arm–gauge interface, which plays a critical role in governing strain uniformity and stress concentration. By allowing the inner profile to vary smoothly from the gauge region into the arm, the formulation minimizes artificial stress localization that may otherwise arise from geometric discontinuities.

The inner arm geometry was fully defined by four independent parameters, one by the fillet radius and the other three spline control parameters, as shown in fig 1. The fillet radius(R) is a concave fillet applied at the immediate junction between the gauge region and the spline curve. This radius enforces curvature continuity at the gauge boundary and influences local stress concentration. Whereas, the spline control-point locations (L1, L2, and L3) define the locations that govern the shape of the inner arm profile. There is a symmetric definition that ensures identical curvature evolution in both loading directions and eliminates geometric bias between the principal axes.

The parameters *R*, L1, L2, and L3 were treated as independent geometric variables, allowing the curvature distribution to be systematically modified without altering the global dimensions of the specimen. This formulation differs from traditional approaches that vary arm width, gauge size, or thickness taper, and instead focuses exclusively on shape control through spline geometry. By parameterizing the geometry in this manner, the study enables (i) smooth and manufacturable transitions, (ii) controlled redistribution of strain gradients, and (iii) direct coupling between geometric parameters and strain-field metrics. The variation of these variables is presented in Table 1. A quarter-symmetry finite element model was used to minimize computational effort while preserving geometric and loading symmetry. Symmetry boundary conditions were applied so that both the geometry and the loading in the horizontal and vertical directions were identical. This ensured an equi-biaxial response, provided no geometric asymmetry are introduced. Based on these geometric parameterising nine different geometries were modelled based on the L9 orthogonal array suggest by Taguchi method and the nine geometries are presented in the table 2.

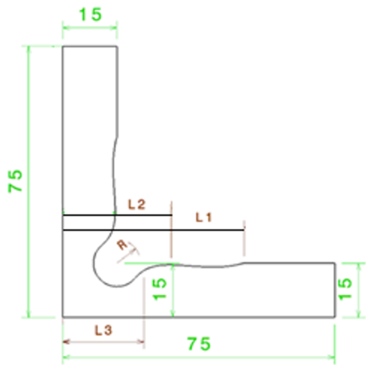

Figure 1: Specimen geometry showing design parameters R, L1, L2, and L3.

Table 1: Geometric parameterising

Parameter	Level 1	Level 2	Level 3	Units
Radius (R)	1.5625	3.25	6.5	mm
L1	50	47.5	45	mm
L2	35	32.5	30	mm
L3	20	22.5	25	mm

Table 2: Geometric parameters suggested by L9 orthogonal array

Run	Geometry	Radius	L1	L2	L3
1	G1	1.5625	50	35	25
2	G2	1.5625	47.5	32.5	22.5
3	G3	1.5625	45	30	20
4	G4	3.25	50	32.5	20
5	G5	3.25	47.5	30	25
6	G6	3.25	45	35	22.5
7	G7	6.5	50	30	22.5
8	G8	6.5	47.5	35	20
9	G9	6.5	45	32.5	25

3. Finite Element Modeling

Finite element simulations were performed using ABAQUS to evaluate the strain-field quality of each cruciform geometry under in-plane biaxial loading. A quarter-symmetry model, as already mentioned, was adopted to reduce computational time while preserving geometric and loading symmetry. The material was modeled as a laminated composite, and the analysis was conducted under quasi-static loading conditions. The same (i) analysis procedure, (ii) material definition, and (iii) output requests were applied to all geometries to enable direct comparison across the design set. Symmetry boundary conditions were imposed along the two principal orthogonal planes to enable a quarter-model representation of the cruciform specimen. On each symmetry plane, the displacement component normal to the plane was constrained to zero, thereby enforcing kinematic compatibility and eliminating artificial rigid-body motion while preserving the mechanical equivalence of the full geometry.

In-plane biaxial loading was applied through displacement-controlled boundary conditions prescribed at the loading boundaries of the specimen arms. Displacement control was adopted to ensure numerical stability, particularly in the presence of progressive stiffness degradation, and to promote uniform and consistent strain evolution within the gauge region across different geometric configurations. The loading was configured to generate an equi-biaxial response, with identical displacement magnitudes applied along both principal loading directions. This ensured a 1:1 loading ratio ($\sigma_x = \sigma_y$), consistent with the geometric symmetry of the cruciform specimen and the intended biaxial stress state.

A consistent and geometry-invariant meshing framework was adopted across all design candidates to eliminate discretization-induced bias in the computed strain-field metrics. Structured refinement was applied within the arm–gauge transition zone and the central gauge region, where strain uniformity serves as the primary optimization objective. Regions away from the gauge were discretized using a comparatively coarser mesh to maintain computational efficiency without influencing the evaluation domain. Particular attention was given to curvature-sensitive regions defined by the spline-controlled arm–gauge transition. For geometries exhibiting increased local curvature (i.e., reduced effective fillet radius or sharper transition gradients), targeted local mesh refinement was introduced to preserve element aspect ratio, maintain Jacobian quality, and mitigate distortion-induced numerical artifacts in the extracted strain field.

All models employed SC8R continuum shell elements with reduced integration. An element size of 0.6 mm was imposed uniformly within the gauge region to ensure consistent strain resolution across geometries. Mesh density, element distortion metrics, and integration stability were monitored to guarantee comparable numerical accuracy throughout the design set. For each configuration, field outputs were extracted from ABAQUS and exported as tabulated datasets containing spatial coordinates (x, y, z), element and node identifiers, in-plane strain components (ε_{11}, ε_{22}, ε_{12}), maximum in-plane principal logarithmic strain, corresponding stress components (σ_{11}, σ_{22}, σ_{12}) or (S_{11}, S_{22}, S_{12}), and maximum in-plane principal stress. Critically, ply-level results were retained rather than through-thickness averaged quantities. This ensured that strain-field quality metrics reflect the true laminated composite response, avoiding artificial smoothing of local maxima or curvature-driven strain gradients. Since the optimization objective is defined in terms of strain-field uniformity within the gauge region under equi-biaxial loading, ply-resolved outputs provide a conservative and physically meaningful basis for geometric comparison, particularly when curvature effects vary across candidate designs.

3.1 Gauge Region Definition

The gauge region in each finite element model was defined using geometry-relative coordinate bounds rather than fixed global coordinates. Specifically, the gauge was taken as the region satisfying $X \in [0, 20]$ mm and $Y \in [0, 20]$ mm. The geometry-relative definition ensures that all nine configurations are evaluated on a consistent and physically meaningful basis. All metrics were computed exclusively on elements, corresponding to the outermost surface ply. This choice reflects experimental reality: digital image correlation (DIC), which is the primary strain measurement technique in biaxial testing, measures the specimen surface. Reporting metrics from interior plies would therefore misrepresent the measurable field. For each element in the gauge region, the stress and strain components were first averaged across the element's integration points within first ply, yielding one representative value per element. All subsequent statistical calculations were performed on this element-level dataset.

3.2 Biaxial Suitability Metrics

Each geometry was characterised by five quantitative metrics, (i) stress uniformity, (biaxiality ratio uniformity, (iii) Surface strain uniformity, (iv) Stress concentration factor and (v) Outside-gauge failure count. Collectively, these five metrics would capture three most important attributes of a biaxial cruciform specimen. These attributes are (i) stress field quality, (ii) junction integrity, and (iii) the failure behaviour.

(i) Stress uniformity (CV_S): This factor describes the coefficient of variation of stress S_{11} and S_{22} across all elements in the gauge region which was computed as:

$$CV_S = \frac{1}{2}\left(\frac{\sigma(S11_{el})}{\mu(S11_{el})} + \frac{\sigma(S22_{el})}{\mu(S22_{el})}\right) \times 100\%$$

Where σ and μ denote the standard deviation and mean taken through along the element-level values in the gauge. A low CV_S specifies that the load applied yields to a uniform stress state, which is a qualification for reliable property abstraction.

(ii) Biaxiality ratio uniformity (CV_R): The local biaxiality ratio for each element was calculated by $r_{el} = S_{22}/S_{11}$. Where the CV_R across the elements in the gauge region is given by:

$$CV_R = \frac{\sigma(r_{el})}{\mu(r_{el})} \times 100\%$$

Biaxiality ratio uniformity (CV_R) is possibly more significant than CV_S alone, as it processes if elements in the gauge experiences the same stress state. Whereas, CV_S identify whether the individual stress components are uniform independently. That means that even if S_{11} and S_{22} are individually uniform, a spatially varying ratio would mean that different parts of the gauge are under different biaxial conditions, compromising the validity of failure envelope measurements.

(iii) Surface strain uniformity (CV_{LE}): This is the coefficient of variation of the logarithmic strains LE_{11} and LE_{22} on the surface of the ply, was calculated similar to that of CV_S. This metric directly predicts the strain distribution very similar to the DIC measurement quality. A non-uniform strain field yields to a spatially averaged DIC reading that undervalues the true peak strain, which leads to an un-conservative material response.

(iv) Stress concentration factor (SCF): The SCF at the arm–gauge intersection is defined as the ratio of the ultimate elemental mean stress S_{11} in the arm section in the proximately of the gauge region to the ultimate elemental mean stress S_{11} across all gauge elements:

$$SCF = \frac{max(S11_{arm})}{\mu(S11_{gauge})}$$

The arm area was defined as X ∈ [X_min + 20, X_min + 25] mm, strictly outside the gauge region. An SCF significantly above 1.0 specifies that the intersection is of high stress that might fail earlier to the gauge region, generating an unacceptable condition. The SCF was intentionally calculated using the arm-side stress rather than the gauge area, in order to avoid insincerely expanding the metric by with the gauge corner region.

(v) Outside-gauge failure count (Nout): For all geometries, the Hashin matrix tension criterion HSNMTCRT ≥ 1.0 were identified for all elements across all plies reaching. Which were later classified as failure being inside or outside the gauge region. This count of unique outside-gauge failed elements, N_{out}, is a binary in nature. This means any geometry disqualifies if $N_{out} > 0$, which is considered as unsuitable for experimental testing, as it indicates that the specimen will fail in the arm region rather than the gauge. This helps in interpreting the test as invalid irrespective of how good the stress uniformity metrics are.

3.3 Composite Scoring

To rank the valid geometries, a composite score was calculated by normalising each metric to the range [0, 1] across all geometries and forming a weighted sum:

$$Score = w_1\tilde{CV}_S + w_2\tilde{CV}_R + w_3\tilde{CV}_{LE} + w_4\widetilde{SCF} + 2.0 \cdot \tilde{N}_{out}$$

Where the tilde denotes min-max normalisation, and the weights $w_1 = 0.30$, $w_2 = 0.25$, $w_3 = 0.20$, $w_4 = 0.25$ reflect the relative experimental importance of each criterion. The factor of 2.0 applied to N_{out} acts as a strong penalty that pushes any geometry with outside-gauge failures to the bottom of the ranking, irrespective of its uniformity metrics. A lower composite score indicates a more suitable geometry.

4. Results and Discussion:

The finite element analysis depicts three distinctly different performance tiers among the nine cruciform configurations. The general characteristics of the stress field topology should be described prior to making specific measurements, as they will form the basis upon which quantitative comparisons can be evaluated. Across all measurement configurations, the dominant in-plane stress component is S_{11}, the fiber direction stress, throughout the gauge. S_{22}/S_{11} (the gauge mean biaxiality ratio) is 0.1566 in G2, 0.1560 in G1, and 0.1564 in G3. All measurements have been made under equal displacement boundary conditions being applied to all four of the gauge arms. Biaxiality ratios decrease to between 0.149 and 0.151 in Tier 2 and between 0.147 and 0.148 for rejected geometries, all indicating a much lower transverse stress than S_{11}. The sub-unity ratio of S_{22}/S_{11} results from the anisotropic laminate material made of glass and epoxy and equibiaxially applied displacement. For example, when there are symmetric kinematics, there still is a large difference in the stiffness (E_{11} to E_{22}), which creates an inherently uneven response from a stress standpoint. This relationship creates no load imbalance. The PLY-1 logarithmic strain components, LE_{11} and LE_{22}, have numerically equivalent values within .0001 across all geometries ($LE_{11} = LE_{22} = 3.878°$ for g2). This establishes that inequality within S_{11} and S22 is a constitutive property of the material rather than a result of modelling, as well as confirming that the imposed boundary conditions provide a true equibiaxial strain state.

Throughout all geometries, in-plane shear stress (S_{12}) is almost non-existent throughout the gauge interior and increases in proximity to the re-entrant arm-gauge corners; thus, confirming that the imposed symmetry boundary conditions do not artificially introduce shear into the measurement zone, thereby supporting the assumptions used in the quarter-symmetry model to describe the mechanical behaviour of PLY-1 material.

4.1 Stress Field Contours

Nine geometries on each of the first ply surfaces showed the global direction of the fibers stress S_{11}, transverse stress S_{22}, in-plane shear stress S_{12}, and also the biaxiality ratio S_{22}/S_{11} distribution, and the matrix tensile failure damage index HSNMTCRT. The three highest-ranked and three lowest-ranked geometries (G1, G2, G3) exhibit very distinct behaviours when comparing the S11 contours. The stress here appears to be elevated over a relatively small band immediately adjacent to the arm/gauge junction corner, as there is a largely consistent yellow area over the interior of the gauge; whereas the G4, G5, and G6 geometries exhibit a large increase in these stresses from the centre of the gauge out to the edge (suggesting that the transition profiles for these configurations allow for non-uniform redistribution of stresses). Geometries G7, G8, and G9 show the most severe gradients, with elevated S_{11} penetrating well into the gauge interior from the junction corner.

The comparative visualizations of both loading conditions (during application of the same biaxial axial force) can also be evaluated using the S_{22}/S_{11} biaxiality ratios (refer to Fig. 2). The S_{22}/S_{11} biaxiality ratio for each of the nine geometries is reported to be approximately 0.157 throughout the central gauge region of the specimen indicating that the predicted results according to classical laminate theory are accurate and the material exhibits intrinsic anisotropy, thus supporting the conclusion that the load distribution applied does not have a significant effect on the ratio reported above. There are differences in the spatial constancy of the ratio between geometries. The ratio is nearly equal across the majority of the G1 and G2 gauges and only has a localized drop at the free-edge corner where S_{22} approaches zero. This is a well-established free-edge effect and happens in all geometries. The radial gradient of G4, G5, and G6 shows a significant difference in the biaxial condition of elements near the gauge border compared to those located in the centre. Therefore, the spatial variation of the stress ratio has a direct effect on the validity of any failure criteria established on the basis of a uniform biaxial condition. This is what CV_R measures.

Shear stress is almost entirely absent from the center shear gauge at all nine geometries as anticipated by the analysis of the S_{12} shear maps, and only increases near the corner between the arm and gauge as a result of the geometric limitations of the transition region. This behaviour confirms that the boundary conditions have been applied appropriately and is consistent with the assumption of quarter-symmetry.

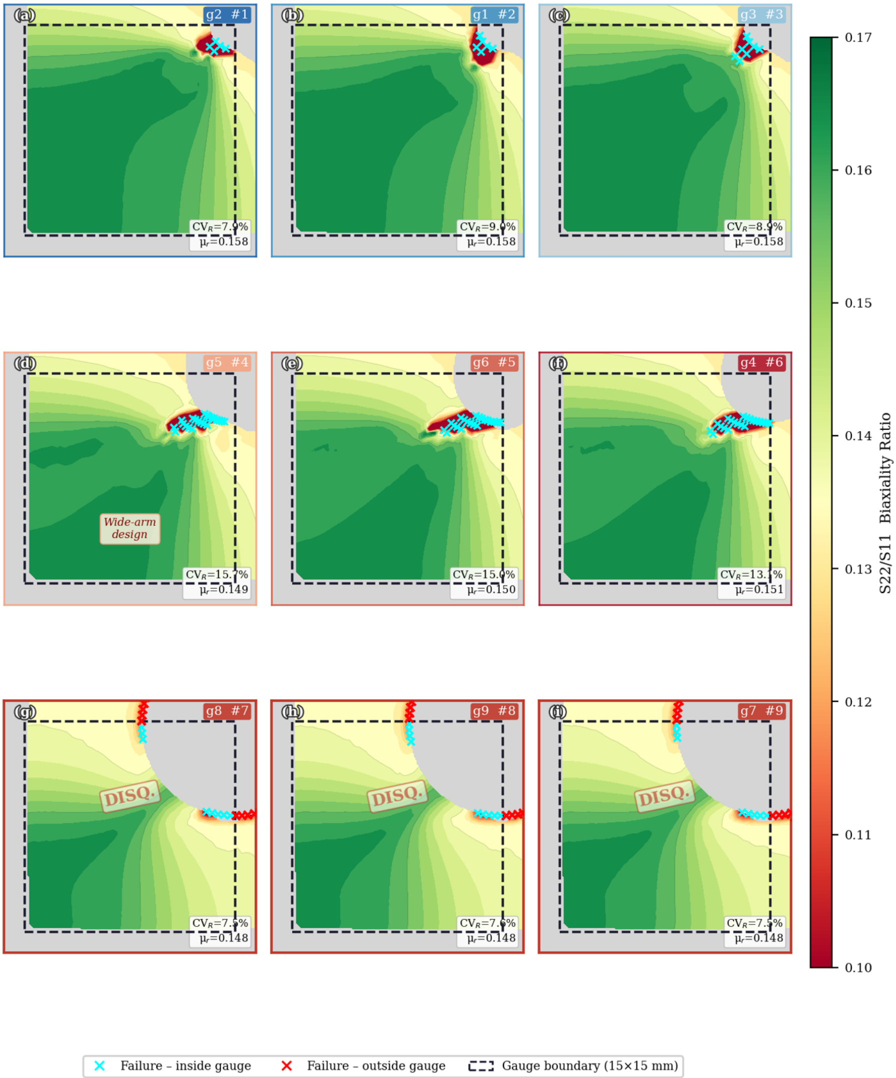

Fig2: S_{22}/S_{11} biaxiality ratio distribution for all nine cruciform configurations ranked by composite suitability score.

4.2 Quantitative Metric Comparison

Table 3 contains the five suitability metrics and total (aggregate) scores for the nine configurations in this study. The outside-gauge failure criteria (N_{out} = 75, 65, and 55, respectively) immediately eliminate three of the geometries from consideration (G7, G8, and G9). The geometric configurations that remain will be ranked based on the composite score.

Table 3: Biaxial suitability metrics for all nine cruciform configurations (PLY-1 surface, gauge region)

Rank	Geo	CV_S11 (%)	CV_S22 (%)	CV_S avg (%)	CV_R (%)	CV_LE (%)	SCF	N_in	N_out	Score
1	**G2**	8.93	7.78	**8.36**	7.86	9.72	1.498	25	0	0.014
2	**G1**	8.99	8.45	**8.72**	8.97	9.83	1.492	30	0	0.062
3	**G3**	10.62	9.89	**10.26**	8.94	11.46	1.507	40	0	0.160
4	**G5**	15.04	16.72	**15.88**	15.68	16.02	1.504	107	0	0.679
5	**G6**	16.06	16.53	**16.30**	15.01	17.02	1.799	105	0	0.789
6	**G4**	16.88	15.48	**16.18**	13.13	17.88	2.195	102	0	0.871
—	**G8**	17.04	11.39	**14.21**	7.49	18.04	2.143	50	**55**	2.079
—	**G9**	17.64	11.52	**14.58**	7.55	18.65	2.291	45	**65**	2.421
—	**G7**	16.55	10.94	**13.74**	7.46	17.54	2.289	40	**75**	2.628

N_{in} = failed elements inside the gauge; N_{out} = failed elements outside the gauge. Geometries G7, G8, G9 are disqualified ($N_{out} > 0$).

The data presented in Table 3 (Figure 3) demonstrates three different levels of performance. A complete absence of off-gauge failures from the first tier (G1, G2, G3) results in CV_S values all less than 10.3%, CV_R values all less than 9.0%, and SCF values all less than 1.51; a substantial difference from the second tier which contains G4, G5, and G6 with their respective CV values ranging from 13% to 18% (both CV_S and CV_R)—that is nearly double tier one—and SCF scores of 2.20 for g4 as compared to g2 suggesting a much less consistent Gauge Field and hence greater risk for excessive concentration of junctions along a given arm. Due to all three elements of the third tier experiencing off-gauge failure (G7, G8, G9) all of the elements within the third tier had 55 - 75 HSNMTCRT → 1.0 in the arm area.

The fact that (G7, G8, and G9) produce comparable CV_R values to those in tier 1 (7.46 – 7.55%) demonstrates a significant weakness of using one metric in isolation; there's no assurance that a geometry's bias and bias ratios are accurately reflected in any of the other four criteria, especially because all five criteria have been used to rank the various geometries based on the composite scoring methodology, which combines a total of five quantitative criteria, thus revealing discrepancies in the results of the five criteria for each of the various geometries with respect to one another.

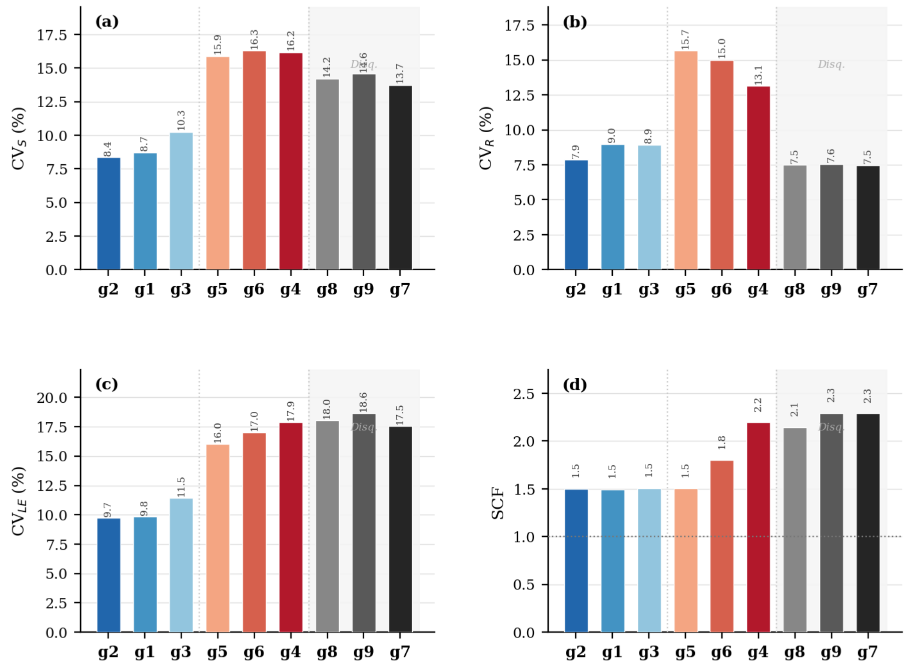

Fig 3: Comparison of suitability metrics for all nine cruciform configurations: (a) stress uniformity CV_S, (b) biaxiality ratio uniformity CV_R, (c) surface strain uniformity CV_{LE}, and (d) stress concentration

4.3 Failure Analysis

The Hashin criteria HSNMTCRT activates matrix tension, which is the predominant failure mechanism in all nine geometries. Fibre tension and compression criteria remained well below 1.0 throughout, which is consistent with the transverse-loading nature of the biaxial stress state for this GFRP layup. Failure mostly starts on PLY-1, the outermost surface ply, and spreads inside to PLY-2 and the symmetric plies at greater stress levels, according to the ply-by-ply breakdown of failed pieces. Twenty of the twenty-five failed components for geometry G2 are in PLY-1, whereas just three are in PLY-2 and two are in Sym_PLY-2, indicating that the damage is really surface-initiated. This is physically compatible with the concentration of free-edge stress at the gauge corner, where shear S_{12} and transverse stress S_{22} work together to push. At the gauge corner, the concentration of free-edge stress is electrically and physically compatible with the gauge (i.e., the way we measure the amount of force acting along a) corner where outer layer matrix cracking produced from the combination of S_{22} transverse stress and S_{12} shear stress.

The area containing all of the failed items for valid geometries is solely confined to the specific area in which the failed parts of G2 lie (i.e., the left-hand gauge corner closest to the juncture where the two arms of the structure come together). The limited area of X values between 14.49 mm and 15.27 mm and Y values between 13.49 mm and 13.69 mm (centroid approximately equal to (14.76 mm to 13.59 mm)) for G2 demonstrates that this portion is directly within the boundary limit of the quarter-gauge creating an area. The distribution of areas for G1 and g3 is similar in that the respective coordinates of the failed areas for G1 and G3 are at (13.72 mm, 13.72 mm) and (13.42 mm, 13.42 mm) compared to G2. Since there is a common area of failure for all three geometries at the quarter gauge corners, the conclusion is established that the corner free edge has the largest influence on where failure occurs, while the geometrical alterations made to geometries G1 and G2 from geometry G3 addresses the size of the effects on corner free edge.

The results from Fig. 4 (Severe Cases G2, & G7) show that when there are 55-75 structural elements that have failed but remain within the arm area (not disqualified yet), those elements will, in all disqualified geometries (G7, G8, G9), fully migrate out of the gauge during the test. In contrast to the previous scenario, the weak point in the geometry will now be located in the area of the arm-gauge junction, rather than at the corner of the gauge (due to the qualitative change in specimen behaviour). Therefore, any experimental test on these geometries will fail completely prior to reaching the measurement location and thus have no applicable material data, making these components unsuitable for testing.

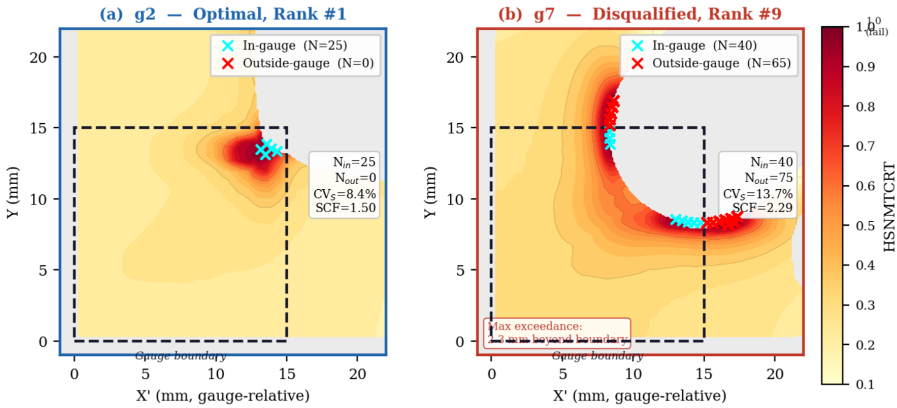

Fig. 4. Hashin matrix tension index (HSNMTCRT) for the optimal geometry g2 (a) and disqualified geometry g7 (b), showing failure location relative to the gauge boundary.

4.4 Optimal Geometry and Practical Implications

With an average CV for stress of just 8.36% (lowest), a CV for the biaxiality ratio of 7.86% (also lowest), and the only strain CV <10% (just 9.72%), a low SCF (1.498), and zero out-of-gauge failures, G2 is by far the best performing design overall across all of these metrics. G2 has a composite score which is the lowest (0.014), significantly outperforming G1 (0.062), which, while still strong, produces very similar stress measurements and failure behaviour as G2.

Aside from FEA analyses, G2 has additional benefits as measured by experimentation. It can accommodate usual servo hydraulic biaxial test rig loads and stroke capacity (S_{11} arm side = 132.5 MPa) with estimated gauge displacements of 0.36 mm. Geometries such as G8 and G9 would require approximately two times the actuator stroke used by G2 (0.64-0.69 mm) and would require greater machine accuracy than G2 with more alignment sensitivity than G2. Although these geometries failed for various reasons, their failure is still of significant concern. There are no special fixtures required because of the similarity between the arm width for all geometries and the use of most conventional hydraulic grip systems meant to hold.

A direct indicator of measurement reliability for DIC strain measurement used for later experimental characterization is provided by the uniformity of surface strain measured using the CV_{LE} parameter. With a CV_LE = 9.72% the G2 geometry has an acceptable level of CV_{LE}'s under the 10% threshold that was determined to be appropriate for DIC based material characterization. Therefore, the average spatial bias associated with DIC will remain typically within reasonable limits for this geometry. If an alternative material configuration produces a CV_{LE} >10% there will be an expectation that DIC measured gauge strains will provide an under estimate of the actual element level failure strains and the bias will increase as the CV_{LE} increases. When comparing the next valid geometry G3 (CV_{LE} = 11.46%) against G2 (CV_{LE} = 9.72%), the difference between these geometries will not only be statistically significant; an experimental test will ultimately yield measurable differences in the strain-at-failure data resulting from these two geometries, thus, having an effect on the accuracy of the progressive damage model(s) calibrated from these measurements.

4.5 Effect of Geometric Parameters

The Taguchi L9 orthogonal array layout simulates a full factorial experiment by providing a means to systematically evaluate the effects of two geometric design parameters (fillet radius and spline transition profile) on the performance of biaxial specimens without requiring a large number of experiments.

A quick comparison between Tier 1 (G1, G2, G3) and Tier 2 (G4, G5, G6) shows there is an instantaneous and drastic change between CV_S and CV_R) for both Configuration. For Tier 1, CV_S and CV_R are both between 8.36% and 10.26% and between 7.86% and 8.94% respectfully respectively, and then both measurements jump up to 15.88% - 16.30% and 13.13 % - 15.68% respectfully for Tier 2. This is equal to more than two times what the measurements are for Tier 1. Instead of resulting in an overall linear response across the nine configurations, this abrupt step does not allow for the expectation of a continuous evolution and is source to one or the other Taguchi parameters exceeding that of the two tiers. The visual evidence commonly supports this conclusion; the Tier 2 geometries display a continual, radial gradient that traverses into the gauge from the junction (Fig. 5d-f); this suggests that the load distribution mechanism causing the change in geometry is fundamentally dissimilar to that causing the Tier 1 geometries. Conversely, the Tier 1 geometries display a largely uniform stress distribution within the gauge with stress located in a narrow area throughout the regions of the junction and the gauge arm (Fig. 5a-c).

A different but complementary narrative is provided through the SCF. Within Tier 2, the SCF ranges from 1.504 (G5) to 1.799 (G6) and 2.195 (G4)—all are very significantly different values even though they all occur within one tier. In Tier 1, the corresponding values for SCF are 1.492 (G1) and 1.507 (G3), representing an insignificant change across tiers. The SCF exhibits this within-tier variability across configurations having low CV_S values (i.e., low variability), indicating to us that the two parameters independently influence different aspects of the specimen's behaviour: one appears to influence how uniformly gauge stress is distributed throughout the entire region of an assembled joint; and the second appears to influence how much stress is concentrated at the junction between an assembly. Therefore, CV_S optimisation is insufficient because there are cases where a geometry may reach an acceptable level of gauge uniformity while developing a harmful junction concentration based on which parameter is favourably parameterised, or vice versa.

The excluded geometries (G7, G8, and G9) support this idea because their outside-gauge failure modes were caused by a supercritical SCF due to both parameters being at the lowest point or the least favourable level, rather than just by having inadequate stress uniformity (e.g., their CV_R values of 7.46–7.55% are actually comparable to Tier 1). The Taguchi L9 array is specifically designed to reveal this type of interaction effect, i.e., a geometric defect that has catastrophic consequences only when the junctions have both parameters that are unfavourable together.

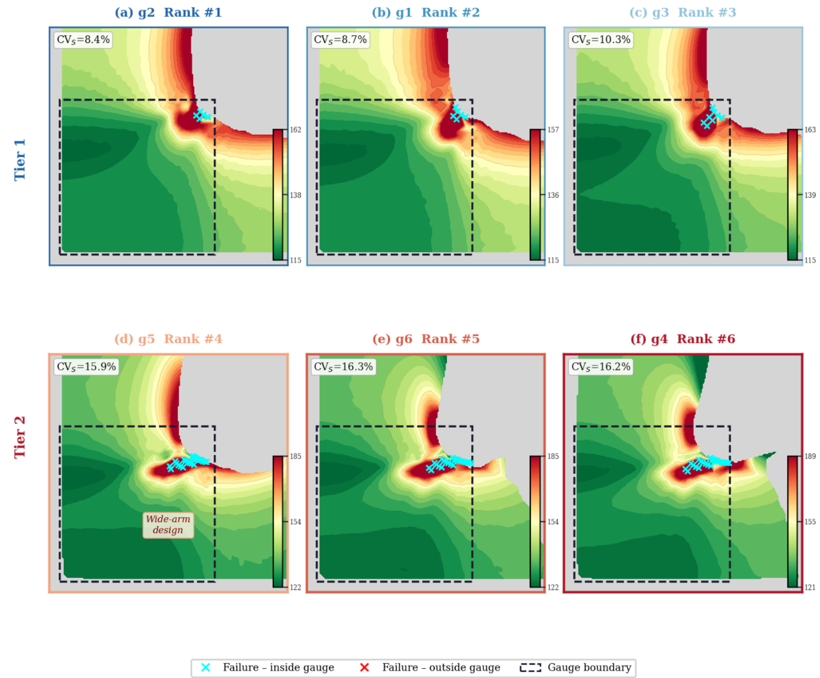

Fig. 5. Fibre-direction stress S_{11} (MPa) for the six valid configurations, grouped by performance tier

Conclusion:

An Optimization Framework has been developed in the present study which uses the Taguchi method. This optimization framework will serve as a basis for future designs supported by this document by producing 9 Different Geometric Configurations of the cruciform specimen using ABAQUS (Finite Element Software) Quarter Symmetry Model, examining the Quality of the Gauge Fields, Evaluating the Junctions Integrity, and measuring the Performance Characteristics of the Specimen using various Quantitative Measurements.

Three out of the nine geometries (namely G7, G8, and G9) were ruled out after being tested due to having Hashin matrix-tension damage from outside the gauge border; therefore, having just a wide fillet radius is not enough to produce appropriate test conditions. Six of the nine geometries that were left were separated into two levels of performance based on stress concentration factor and homogeneity. The first tier of geometries (G1, G2, and G3) demonstrated to be able to achieve a stress CV value of less than 10.3%, a biaxiality-ratio CV value of less than 9.0%, and an SCF value of less than 1.51. The second tier of geometries (G4, G5, and G6) had much less than appropriate gauge fields, being approximately twice as high as the first tier in regards to CV values and reached SCF values of 2.20.

The stress uniformity coefficient-of-variation (CV) of G2's geometry was 8.36%, while its biaxiality-ratio CV was 7.86%, and its surface strain CV was 9.72% (the only surface strain across all nine configurations with a -DIC CV<10% acceptable level). Using the same data, SCF was calculated (1.498) and no external gauge damage was reported. Therefore, G2 rated highest in all five performance categories based upon a combination of all data. Based on its estimated gauge displacement (0.36 mm) and arm width (14.0 mm), direct experimental implementation of G2's geometry is feasible given that both of these dimensions are representative of commonly used servo-hydraulic rigs and hydraulic grips.

This study found that the use of a C^2-continuous spline transition with a small fillet radius resulted in more uniform biaxial stresses than would either an abrupt taper or a circular transition. The composite scoring framework that was used to evaluate the designs based on five metric values demonstrated value in terms of the results from both multi-objective evaluations and single metric rankings, allowing for the identification of geometries that appeared to meet the metric criteria during independent assessment; however, these geometries were not acceptable due to their location of failure.

The work completed as part of this research is based entirely on finite element modelling; experimental validation for G2 and ANOMs are required to quantify the contributions of each of the splines' four control parameters before the design can be recommended for general use.

Acknowledgement: The authors acknowledge the financial support received from the Anusandhan National Research Foundation (ANRF) under the Core Research Grant (CRG) scheme (File No. CRG/2023/004740).

References:

1. Van Paepegem, W., Degrieck, J., & De Baere, I. (2010). Strain distribution in cruciform specimens subjected to biaxial loading conditions. Part 2: Influence of geometrical discontinuities. Polymer Testing, 29(2), 161–170. https://doi.org/10.1016/j.polymertesting.2009.11.006

2. Chen, X., Li, Y., Zhang, H., & Wang, Z. (2022). Designing a Cruciform Specimen via Topology and Shape Optimisations under Equal Biaxial Tension Using Elastic Simulations. Materials 2022, 15(14), 5001; https://doi.org/10.3390/ma15145001

3. Makris, A., Vandenbergh, T., & Van Paepegem, W. (2015). Numerical optimization of cruciform specimens for multiaxial testing. Engineering Fracture Mechanics, 147, 294–309. https://doi.org/10.1016/j.engfracmech.2015.09.018

4. Kim, J. H., Hong, S. G., & Lee, J. H. (2018). Design optimization of cruciform specimens for improved strain homogeneity under biaxial loading. International Journal of Solids and Structures, 144–145, 1–14. https://doi.org/10.1016/j.ijsolstr.2018.04.015

5. Lu, Y., Zhang, X., Chen, Y., & Li, Z. (2020). Optimization of cruciform specimen geometry for biaxial tensile testing using orthogonal experimental design and finite element analysis. Metals, 10(9), 1148. https://doi.org/10.3390/met10091148

6. Deng, J. (2018). Grey relational analysis for multi-response optimization: Principles and applications. Materials, 11(9), 1743. https://doi.org/10.3390/ma11091743

7. Serna Moreno, M. C. S., & Horta Muñoz, S. (2024). Experimental evaluation of the use of cruciform specimens for biaxial stability analysis. Composites Part B: Engineering. https://doi.org/10.1016/j.compositesb.2024.111764

8. Vitucci, G. (2024). Biaxial extension of cruciform specimens: Embedding equilibrium into design and constitutive characterization. Experimental Mechanics, 64, 539–550. https://doi.org/10.1007/s11340-024-01052-2

9. Dexl, F., & Boehler, J. (2023). Numerical optimization-based design studies on biaxial cruciform specimens. Proceedings in Mechanical Engineering Journals.